Journal of Fluids and Structures 130 (2024) 104187

Contents lists available at ScienceDirect

Journal of Fluids and Structures

journal homepage: www.elsevier.com/locate/jfs

Global stability analysis of flow-induced-vibration problems using an immersed boundary method

Zhiyu Zhang, Jianfeng Lu, Xing Zhang *

The State Key Laboratory of Nonlinear Mechanics, Institute of Mechanics, Chinese Academy of Sciences, Beijing 100190, China
School of Engineering Science, University of Chinese Academy of Sciences, Beijing 100049, China

ARTICLE INFO

Keywords:
Global stability analysis
Fluid–structure interaction
Immersed boundary method
Flow-induced vibration
Elastically mounted cylinder

ABSTRACT

In this work, a numerical framework for global stability analysis of rigid-body-motion fluid–structure-interaction problems is presented. The Jacobian matrices which arise in the linearization procedure are derived numerically via the first-order finite difference scheme. The linearized fluid–structure coupled equations are solved using an immersed boundary method. The linear stability solver is first tested on two canonical cases, i.e., the flow past a stationary cylinder and the flow past an isolated elastically mounted cylinder. An excellent agreement between the results obtained here and those from available published research is achieved. The solver is then used to study the linear stability of the flow past two elastically mounted cylinders in tandem arrangement. The variations in growth rate and frequency of two leading modes with reduced velocity are examined. The mechanisms of lock-in and galloping phenomena observed in nonlinear simulation are elucidated from the perspective of linear instabilities in the leading modes.

1. Introduction

Flow-induced vibration (FIV) is a common phenomenon observed in nature and engineering practices. In structures such as tall buildings (Hayashida and Iwasa, 1990; Kawai, 1992) and offshore facilities (Kim et al., 2018; Thorsen et al., 2019), FIV can lead to fatigue damage and cause safety issues. On the other hand, FIV can also be utilized to harvest hydrokinetic and wind energies from the environment (Wang et al., 2020; Zhu et al., 2021).

FIV is a classic bi-directional fluid–structure interaction (FSI) problem. Despite of the fundamentally nonlinear nature, the onset of FIV can be predicted by examining the stability of linearized systems. Global stability analysis is a well-developed method for describing the linear systems and determining the bifurcation thresholds (Theofilis, 2017; Gómez et al., 2012). There is abundant literature on applying this method to fluid systems (such as the wakes of bluff bodies). It was only until recently that the global linear stability analysis was applied to fluid–structure coupled systems.

The transformation of equations to a non-inertial body-fixed frame is a well-established technique to handle moving boundaries in FSI simulation. Naturally, such technique has also been applied to perform global stability analysis of fluid–structure coupled systems. Cossu and Morino (2000) was the first to investigate the linear instability of a canonical FIV model — the flow past a rigid circular cylinder which is free to oscillate in the transverse direction. The result indicated that the first instability can be identified at a Reynolds number that was much lower than the critical value for the onset of vortex shedding in a stationary cylinder. The occurrence of vortex shedding at a subcritical Reynolds number was rationalized by the occurrence of instability in a structural mode. The critical Reynolds number of the FIV system determined by global stability analysis was found to be consistent with the value

* Corresponding author.
E-mail addresses: zhangzhiyu@imech.ac.cn (Z. Zhang), lujianfeng@imech.ac.cn (J. Lu), zhangx@lnm.imech.ac.cn (X. Zhang).

https://doi.org/10.1016/j.jfluidstructs.2024.104187
Received 8 March 2024; Received in revised form 2 August 2024; Accepted 3 September 2024
Available online 11 September 2024

determined via nonlinear simulation by Mittal and Singh (2005). The results of linear stability analysis from Meliga and Chomaz (2011), Zhang et al. (2015), Navrose and Mittal (2016), Kou et al. (2017), Yao and Jaiman (2017) also confirmed that the first instability can be triggered at a subcritical Reynolds number. Navrose and Mittal (2016) investigated the correlation between the lock-in phenomenon and linear instability in the FIV system. Dolci and Carmo (2019) considered the flow past a cylinder which was allowed to oscillate in both transverse and in-line directions, and linear stability analysis was applied to find the critical Reynolds numbers at different combinations of mass ratio and reduced velocity. Subsequently, sensitivity of the least stable mode with respect to the local forces was investigated by the same group (see Dolci and Carmo, 2022). Moulin and Marquet (2021) performed global stability analysis of a more complex FIV system involving a heaving-and-pitching spring-mounted rigid plate, and a parametric exploration was conducted to identify different types of unstable modes.

Additionally, the technique of non-inertial reference frame has also been utilized to examine the stability of the paths in falling (or rising) objects under gravity (or buoyancy). Assemat et al. (2012) investigated the stability of the falling paths in two-dimensional flat plates with different geometric parameters. Subsequently, Tchoufag et al. (2014b) employed a similar approach to study the falling paths of three-dimensional objects (such as disks and thin cylinders). Linear stability analysis was also applied to study the stability of the paths in rising bubbles (e.g., spheroidal bubbles by Tchoufag et al. (2014a) and oblate bubbles by Cano-Lozano et al. (2016)). Vagnoli et al. (2023) investigated the effect of permeability on the stability of the paths in falling objects.

Arbitrary–Eulerian–Lagrangian (ALE) method is another widely used technique in FSI simulations to handle moving and deforming boundaries. The attempts to perform global stability analysis using the ALE method were also found in the literature. Fernández and Tallec (2003a,b) performed linear stability analysis of FSI problems by starting with the ALE equations in a weak form. Following the same methodology, Negi et al. (2020) proceeded with the linearization of ALE equations in a strong form. Pfister et al. (2019), Pfister and Marquet (2020) derived the linearized FSI equations in the ALE framework via a Lagrangian-based approach.

FSI simulation can also be conducted using the immersed boundary (IB) method in which a non-conforming mesh is employed. The IB method thus provides an alternative avenue for performing global stability analysis of FSI problems. The IB method enjoys some specific advantages over the other two methods aforementioned. First, multiple rigid bodies with relative motions with respect to each other or flexible bodies with a large number of degrees of freedom can be easily handled. Obviously, under such circumstances, the technique of non-inertial reference frame is no longer applicable. Second, the IB method uses a stationary mesh and a fixed computational domain. Thus, the complexity in the ALE method associated with the linearization of fluid equations on a deforming domain is circumvented.

Till now, global stability analysis of FSI problems based the IB method is still at its exploratory stage and only a few attempts have been made. Goza et al. (2018) performed global stability analysis of an inverted-flag system and explored the mechanisms that initiated flapping. Tirri et al. (2023) proposed an algorithm in which the analytical derivation of linearized FSI equations can be avoided. They then performed linear stability analysis of a FIV system involving the flow past two tandem elastically mounted cylinders.

In this paper, we perform linear stability analysis on a series of FIV problems by combining the standard matrix-forming linearization procedure with a direct-forcing IB method. The contributions of the present paper are twofold. The first contribution is that a linear stability solver is developed based on a direct-forcing IB method in the streamfunction formulation proposed by Wang and Zhang (2011). The linear stability code is then thoroughly validated with two canonical testing cases, including the flow past a stationary cylinder and the flow past an isolated elastically mounted cylinder. The results of the present study are compared with available data from the literature. A second contribution is that we conduct further investigate on linear stability of the flow past two elastically mounted cylinders in tandem arrangement. Although nonlinear simulations of the dual-cylinder FIV system have been conducted in many previous works, such as Borazjani and Sotiropoulos (2009), Kim et al. (2009), Griffith et al. (2017), Qin et al. (2019), Lin et al. (2020), Hu et al. (2020), Sharma and Bhardwaj (2023), etc., global stability analysis was only found in Tirri et al. (2023). In comparison with the work by Tirri et al. (2023), a much wider parameter range is explored in the present study. The results of present work can help us better understand the mechanisms of lock-in and galloping phenomena observed in nonlinear simulation.

The rest of the paper is organized as follows. The physical model and governing equations are presented in Section 2. In Section 3, the numerical methods for solving the nonlinear and linearized equations are introduced. The results and discussion are provided in Section 4. Finally, some conclusions are drawn in Section 5.

2. Physical model and governing equations

In this study, we consider two rigid circular cylinders which are elastically mounted and immersed in a two-dimensional incompressible viscous flow. The cylinders are free to oscillate in the cross-stream direction. A schematic representation of the physical model is shown in Fig. 1. The two cylinders have the same diameter D, and the streamwise distance between the two centers is L. The flow direction is from left to right and a uniform inflow velocity U_∞ is specified at the left boundary.

The flow is assumed to be laminar and is governed by incompressible Navier–Stokes equations, which can be written in a dimensionless form as

$$\frac{\partial \boldsymbol{u}}{\partial t} + (\boldsymbol{u}\cdot\nabla)\boldsymbol{u} = -\nabla p + \frac{1}{\mathrm{Re}}\nabla^2\boldsymbol{u} + \boldsymbol{f}, \tag{1a}$$

$$\nabla\cdot\boldsymbol{u} = 0, \tag{1b}$$

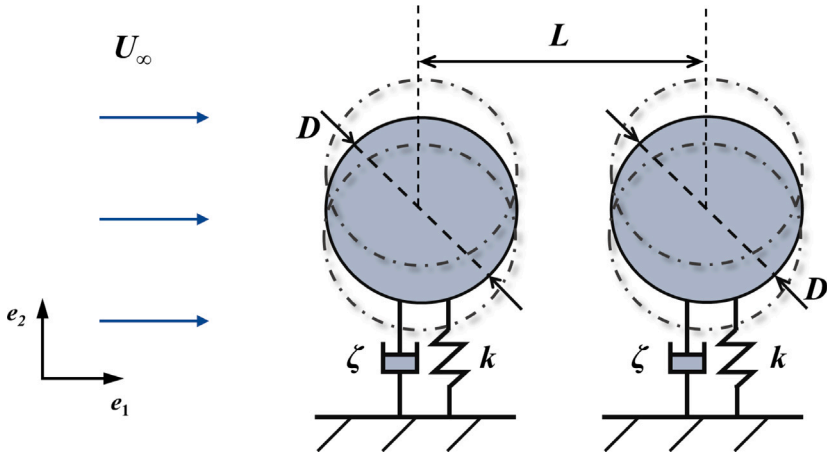

Fig. 1. Schematics of the physical model.

where $\boldsymbol{u}$ is the velocity vector and p is the pressure. $\boldsymbol{f}$ is the body-force term which represents the interaction between the flow and the immersed objects. This term can be implicitly determined by enforcing the no-slip condition on the surfaces of objects.

The motions of the cylinder centers are governed by Newton's second law, which can be written in a dimensionless form as

$$\ddot{Y}_{c,i} + \frac{4\pi\xi}{U^*}\dot{Y}_{c,i} + (\frac{2\pi}{U^*})^2(Y_{c,i} - Y_{c,i}^{eq}) = \frac{4C_{y,i}}{\pi M^*}, \tag{2}$$

where $Y_{c,i}$ and $Y_{c,i}^{eq}$ are the vertical position and vertical equilibrium position of the ith cylinder center. In the present study, $Y_{c,i}^{eq}$ is set to zero. U^* is the reduced velocity, ξ is the dimensionless damping coefficient, and M^* is the density ratio. $C_{y,i}$ is the lift coefficient of the ith cylinder, which is defined as $C_{y,i} = \mathcal{F}_{y,i}/(\rho_f U_\infty^2 D)$, where $\mathcal{F}_{y,i}$ is the vertical component of the resultant hydrodynamic force exerted on the ith cylinder. In the framework of the immersed boundary method for solving Navier–Stokes equations, this hydrodynamic force can be computed using body-force $\boldsymbol{f}$.

The reference length, velocity, and time used in the nondimensionalization are D, U_∞ and D/U_∞, respectively. The dynamic behavior of the FIV system is determined by five dimensionless parameters, namely, Reynolds number Re, reduced velocity U^*, reduced mass M^*, dimensionless damping coefficient ξ and gap ratio G. The definitions of these parameters are:

$$\mathrm{Re} = \frac{DU_\infty}{\nu}, \tag{3a}$$

$$U^* = \frac{U_\infty}{F_n D} = \frac{U_\infty}{D}2\pi\sqrt{\frac{m_s}{k}}, \tag{3b}$$

$$M^* = \frac{\rho_s}{\rho_f}, \tag{3c}$$

$$\xi = \frac{\zeta}{2\sqrt{km_s}}, \tag{3d}$$

$$G = L/D. \tag{3e}$$

Here m_s is the mass of the cylinder, $F_n = \frac{1}{2\pi}\sqrt{\frac{k}{m_s}}$ is the natural frequency of the spring-cylinder system in vacuum, with its dimensionless form f_n defined as $f_n = \frac{F_n D}{U_\infty} = \frac{1}{U^*}$. ρ_f and ρ_s are the densities of the fluid and the cylinders, respectively. ζ and k are the damping coefficient and stiffness coefficient, respectively. In this study, we only consider cases with no structural damping and thus $\xi = \zeta = 0$.

3. Numerical methods

3.1. Nonlinear solver

A direct-forcing immersed boundary method based on discrete streamfunction formulation, which was proposed by Wang and Zhang (2011), is used to solve the incompressible Navier–Stokes equations. In this method, the pressure term is eliminated and the continuity equation is automatically satisfied. The spatially discrete and temporally continuous equations for the fluid flow, the equations for the displacements of cylinder centers and the no-slip boundary condition on the cylinder surfaces can be written as

$$\boldsymbol{C}^{\mathrm{T}}\boldsymbol{C}\dot{s} + \boldsymbol{C}^{\mathrm{T}}\boldsymbol{N}(\boldsymbol{C}s) = \frac{1}{\mathrm{Re}}\boldsymbol{C}^{\mathrm{T}}\boldsymbol{L}\boldsymbol{C}s + \boldsymbol{C}^{\mathrm{T}}\boldsymbol{H}^{\mathrm{T}}(\boldsymbol{X})\boldsymbol{F}, \tag{4a}$$

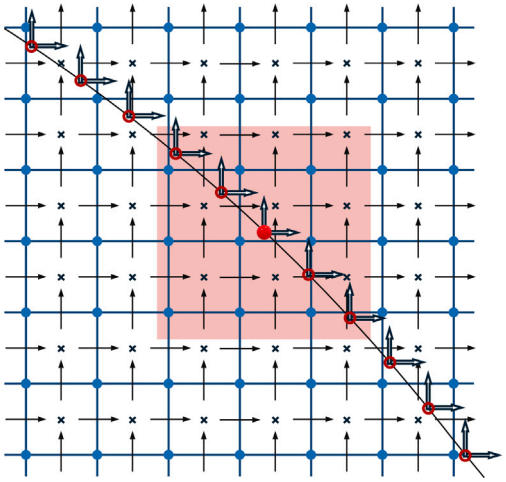

Fig. 2. Schematics of Eulerian and Lagrangian meshes with variable arrangements in a direct-forcing immersed boundary method based on streamfunction formulation. The black curve represents one section of the boundary of an object. The solid blue circles (Eulerian grid points at $\boldsymbol{x}$) represent the locations of discrete stream function s. The horizontal and vertical arrows ($\rightarrow, \uparrow$) represent the locations of two velocity components. The velocity vectors $\boldsymbol{u}$ are defined at each cell center ($\times$). The red circles (Lagrangian grid points at $\boldsymbol{X}$) represent the locations where horizontal and vertical Lagrangian force components ($\Rightarrow, \Uparrow$) are defined. The pink shaded square represents the supporting domain of $\boldsymbol{H}^{\mathrm{T}}(\boldsymbol{X})$ at a selected Lagrangian grid point. (For interpretation of the references to color in this figure legend, the reader is referred to the web version of this article.)

$$\left(1-\frac{1}{M^*}\right)\ddot{Y}_{c,i}+\left(\frac{2\pi}{U^*}\right)^2 Y_{c,i}=\frac{4[\sum(\boldsymbol{F}\cdot\boldsymbol{e}_2)\Delta s]}{\pi M^*}, \tag{4b}$$

$$\boldsymbol{H}(\boldsymbol{X})\boldsymbol{C}s=\dot{\boldsymbol{X}}=\dot{Y}_{c,i}\boldsymbol{e}_2. \tag{4c}$$

Here s is the discrete streamfunction, $\boldsymbol{C}$ and $\boldsymbol{C}^{\mathrm{T}}$ are two discrete curl operators mimicking $\nabla\times(\cdot)$, $\boldsymbol{N}$ and $\boldsymbol{L}$ are the discrete convection and discrete diffusion (Laplacian) operators, respectively. In constructing the discrete operators above, the spatial derivatives are approximated with the standard second-order finite difference scheme.

In Eq. (4), $\boldsymbol{X}$ denotes the position vectors of the Lagrangian points. $\boldsymbol{F}$ represents the Lagrangian forces which are defined on the Lagrangian points. The arrangements of variables on a staggered Cartesian mesh and a Lagrangian mesh are illustrated in Fig. 2. $\boldsymbol{H}^{\mathrm{T}}(\boldsymbol{X})$ and $\boldsymbol{H}(\boldsymbol{X})$ are two discrete operators based on discrete delta function for interpolating Lagrangian forces to the Eulerian grid points and interpolating Eulerian velocity components to the Lagrangian points, respectively. More specifically, the three-point smoothed delta function is adopted in the present study (Yang et al., 2009). For the details, please refer to Wang and Zhang (2011) and Zhu et al. (2014).

At each time step in the solution of Eq. (4), $\boldsymbol{F}$ is determined by an incremental correction method via enforcing the no-slip boundary condition Eq. (4c). Tests on some canonical cases indicated that the velocity errors (i.e., slip and penetration) on the surfaces of immersed objects are sufficiently small by following such procedure (see Wang and Zhang, 2011 for details). This method is in some way different from the generalized projection approach proposed in Taira and Colonius (2007) and Colonius and Taira (2008), where matrix decomposition was performed.

For the temporal advancement of Eq. (4a), the diffusion term is treated using the second-order Crank–Nicolson scheme, while the convection term is treated using a two-stage Runge–Kutta scheme.

Since the cylinders undergo a rigid-body motion, $\boldsymbol{X}$ is time-dependent and must be determined by solving Eq. (4b). On the right-hand side of Eq. (4b), $\boldsymbol{e}_2$ denotes the unit vector in the vertical direction and Δs is the spacing of the Lagrangian mesh. The hydrodynamic force is computed by the summation of Lagrangian forces $\boldsymbol{F}$. Please note that the coefficient of the first term in the left-hand side of Eq. (4b) is different from that in Eq. (2). Such difference arises from the correction needed in the IB method to compensate for the motion of 'pseudo fluid' enclosed by the surface of the cylinder (please see Uhlmann, 2005).

A loosely-coupled scheme is used in the simulation of the FSI problem. Eq. (4b) is solved by converting it into two first-order differential equations. By defining the vertical velocity of the ith cylinder center as $V_{c,i}=\dot{Y}_{c,i}$, the temporal advancement of Eq. (4b) can expressed as

$$V_{c,i}^{n+1}=V_{c,i}^{n}+\Delta t\frac{M^*}{1-M^*}\left(\frac{4[\sum(\boldsymbol{F}^n\cdot\boldsymbol{e}_2)\Delta s]}{\pi M^*}-\left(\frac{2\pi}{U^*}\right)^2 Y_{c,i}^{n}\right), \tag{5a}$$

$$Y_{c,i}^{n+1}=Y_{c,i}^{n}+\Delta t V_{c,i}^{n+1}, \tag{5b}$$

where $n+1$ and n are the time indexes and Δt is the time-step size.

3.2. Global linear stability solver

Here we assume that the state of the FIV system is $\boldsymbol{q} = [s, V_{c,i}, \boldsymbol{X}, \boldsymbol{F}]^{\mathrm{T}}$. The solution of the FIV system can be decomposed into a base solution and a perturbation as $\boldsymbol{q} = \boldsymbol{q}_b + \boldsymbol{q}'$, where the subscript b and superscript $'$ denote variables of the base solution and the perturbation, respectively (i.e. $\boldsymbol{q}_b = [s_b, 0, \boldsymbol{X}_b, \boldsymbol{F}_b]^{\mathrm{T}}$, $\boldsymbol{q}' = [s', V'_{c,i}, \boldsymbol{X}', \boldsymbol{F}']^{\mathrm{T}}$). The base solution of the FIV system is equivalent to a steady flow past stationary cylinders, and the perturbation is a small disturbance imposed on the system. The governing equations for the perturbation of the FIV system can be obtained by linearizing the original equations around the base solution. The linearized equations for the perturbation can be written as

$$\boldsymbol{C}^{\mathrm{T}}\boldsymbol{C}\dot{s}' + \boldsymbol{C}^{\mathrm{T}}\boldsymbol{N}^{(\ell)}(s_b)\boldsymbol{C}s' = \frac{1}{\mathrm{Re}}\boldsymbol{C}^{\mathrm{T}}\boldsymbol{L}\boldsymbol{C}s' + \boldsymbol{C}^{\mathrm{T}}\boldsymbol{H}^{\mathrm{T}}\left(\boldsymbol{X}_b\right)\boldsymbol{F}' + \boldsymbol{C}^{\mathrm{T}}\left.\frac{\partial \boldsymbol{H}^{\mathrm{T}}(\boldsymbol{X})}{\partial \boldsymbol{X}}\right|_{\boldsymbol{X}=\boldsymbol{X}_b}\boldsymbol{F}_b\boldsymbol{X}', \tag{6a}$$

$$\left(1 - \frac{1}{M^*}\right)\dot{V}'_{c,i} + \left(\frac{2\pi}{U^*}\right)^2 Y'_{c,i} = \frac{4[\sum(\boldsymbol{F}'\cdot\boldsymbol{e}_2)\Delta s]}{\pi M^*}, \tag{6b}$$

$$\dot{Y}'_{c,i} = V'_{c,i}, \tag{6c}$$

$$\boldsymbol{H}\left(\boldsymbol{X}_b\right)\boldsymbol{C}s' + \left.\frac{\partial \boldsymbol{H}(\boldsymbol{X})}{\partial \boldsymbol{X}}\right|_{\boldsymbol{X}=\boldsymbol{X}_b}\boldsymbol{C}s_b\boldsymbol{X}' = \dot{\boldsymbol{X}}' = V'_{c,i}\boldsymbol{e}_2, \tag{6d}$$

where $\boldsymbol{N}^{(\ell)}$ is the linearized convection operator. It should be noted that both the Lagrangian forcing $\boldsymbol{F}$ and the position vector $\boldsymbol{X}$ need to be perturbed in the linearization procedure.

Eq. (6a) represents the linearized momentum equation of the fluid flow, while Eqs. (6b)–(6d) are the linearized structural equations and linearized boundary condition at the cylinder surfaces. The elements in the two Jacobian matrices $\frac{\partial \boldsymbol{H}^{\mathrm{T}}(\boldsymbol{X})}{\partial \boldsymbol{X}}$ and $\frac{\partial \boldsymbol{H}(\boldsymbol{X})}{\partial \boldsymbol{X}}$ which arise in the linearization procedure are approximated with a first-order finite difference scheme (see Goza et al., 2018). More specifically, the kth column of $\frac{\partial \boldsymbol{H}^{\mathrm{T}}(\boldsymbol{X})}{\partial \boldsymbol{X}}$ can be approximated by $\frac{\boldsymbol{H}^{\mathrm{T}}(\boldsymbol{X}_b+\varepsilon\mathbf{e}_k)-\boldsymbol{H}^{\mathrm{T}}(\boldsymbol{X}_b)}{\varepsilon}$, where $\mathbf{e}_k$ is the unit vector in the kth direction and ε is a small real scalar. In the present study, ε is set to 10^{-5}. The results are found to be insensitive to the value of ε, in the range of $10^{-6} \le \varepsilon \le 10^{-3}$.

The linearized equations of the FIV system (i.e. Eq. (6)) can be written in a more concise matrix form as

$$\boldsymbol{B}\frac{\partial \boldsymbol{q}'}{\partial t} = \boldsymbol{A}(\boldsymbol{q}_b)\boldsymbol{q}'. \tag{7}$$

By using the normal-mode assumption $\boldsymbol{q}' = \hat{\boldsymbol{q}}(\boldsymbol{x}, \boldsymbol{X})e^{\lambda t}$, the solution of the linearized equations can be expressed as that of a generalized eigenvalue problem $\lambda\boldsymbol{B}\hat{\boldsymbol{q}} = \boldsymbol{A}\hat{\boldsymbol{q}}$. This generalized eigenvalue problem is then solved by a shift-invert method using PETSc and SLEPc libraries (Balay et al., 2024; Hernandez et al., 2005). The tolerance for the convergence of computed eigenvalues and eigenvectors is set to 10^{-8} in the present study.

The base solution of the FIV system (i.e., a steady flow past stationary cylinders) is obtained by solving the steady-state nonlinear equations Eq. (4) using the Newton–Raphson method. The solution procedure is considered to be converged when the difference between two consecutive iterations is less than 10^{-8}.

It is worthy mentioning that the method proposed in this work can be generalized to tackle three-dimensional FIV systems (e.g. Govardhan and Williamson, 2005, Jauvtis et al., 2001, Rajamuni et al., 2020). The immersed boundary method of Wang and Zhang (2011) is capable of handling three-dimensional geometries. In principle, the derivation of linearized equations in the present work is also valid in a three-dimensional situation.

4. Validation and results

In this section, the code validation tests are presented first. The validation tests include linear stability analyses of the flow past a stationary cylinder and the flow past an isolated elastically mounted cylinder. After that, the result of linear stability analysis on the flow past two tandem elastically mounted cylinders is presented.

4.1. Linear stability of the flow past a stationary cylinder

In the linear stability analysis of the flow past a stationary cylinder, no structural motion is involved. Thus, the linearized equations degenerate into a much simpler form as

$$\boldsymbol{C}^{\mathrm{T}}\boldsymbol{C}\dot{s}' + \boldsymbol{C}^{\mathrm{T}}\boldsymbol{N}^{(\ell)}(s_b)\boldsymbol{C}s' = \frac{1}{\mathrm{Re}}\boldsymbol{C}^{\mathrm{T}}\boldsymbol{L}\boldsymbol{C}s' + \boldsymbol{C}^{\mathrm{T}}\boldsymbol{H}^{\mathrm{T}}\left(\boldsymbol{X}_b\right)\boldsymbol{F}', \tag{8a}$$

$$\boldsymbol{H}\left(\boldsymbol{X}_b\right)\boldsymbol{C}s' = 0. \tag{8b}$$

A non-uniform Cartesian mesh on a computational domain of $[80D \times 56D]$ is used to perform nonlinear simulation and linear stability analysis (see Fig. 3). The mesh is stretched in such a way that the minimum grid spacing of $0.02D$ is uniformly distributed in a small region of $[10D \times 4D]$ around the cylinder, while the maximum grid spacing of $0.55D$ is attained near the domain boundaries.

The boundary conditions in the nonlinear simulation are as follows. At the inlet, a uniform streamwise velocity with zero crosswise velocity is prescribed. At the top and bottom walls, a slip-wall boundary condition is enforced. At the outlet, the constant

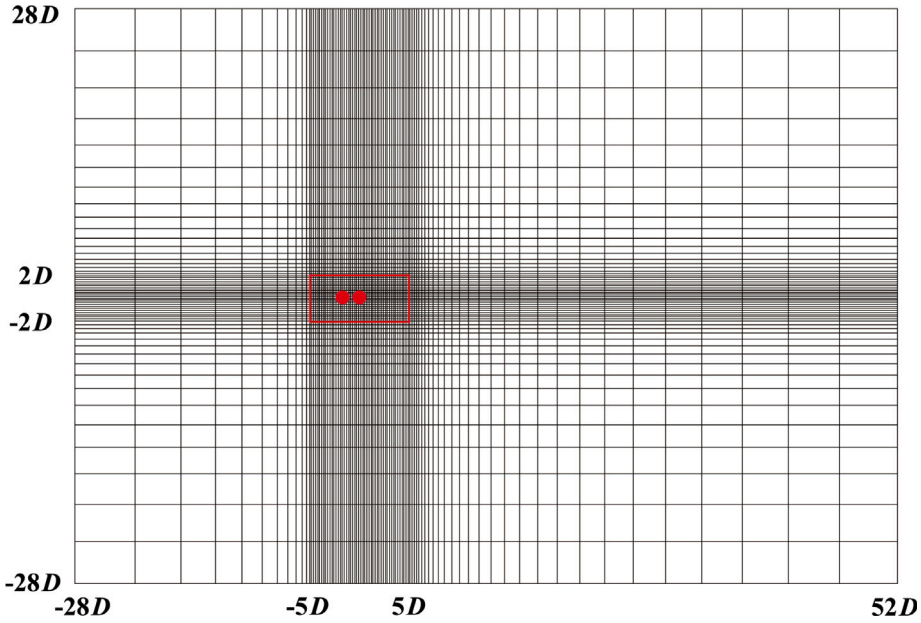

Fig. 3. Schematics of computational domain and mesh used in the simulation.

Table 1
Comparison of eigenvalues predicted in the present study and some reference solutions for the flow past a stationary cylinder.

Re	Present	Giannetti and Luchini (2007)	Relative error
48	0.006+0.734i	0.006+0.744i	1.34%
100	0.123+0.727i	0.123+0.737i	1.32%

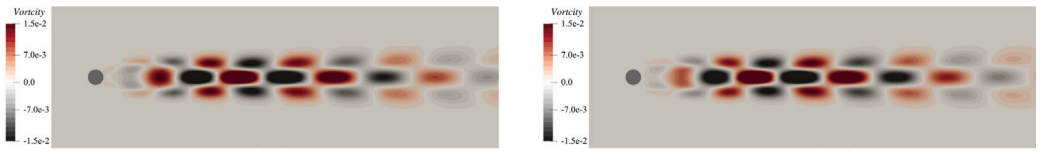

(*a*) (*b*)

Fig. 4. Vorticity field of the real part of the leading eigenmode for the flow past a stationary cylinder at Re=100.

pressure condition is imposed. A fixed time-step size, which ensures that the CFL number is lower than 0.5, is used in temporal advancement. In the linear stability analysis, zero velocity perturbation is prescribed at the inlet and the two side walls. At the outlet, the condition of constant pressure perturbation is prescribed. Convergence tests have been conducted to guarantee that the mesh resolution and domain size are sufficient for obtaining accurate results.

The linear stability property of cylinder wake has been extensively investigated. The critical Reynolds number for the onset of vortex shedding obtained here is $\mathrm{Re}_c = 46.4$. This value is very close to the ones obtained in the existing literature. The results of linear stability analysis for the case of Re = 50 (where the Reynolds number is slightly higher than Re_c) and the case of Re = 100 (where the Reynolds number is much higher than Re_c) are presented here. The eigenvalues of the unstable modes in the two cases are compared with the results from Giannetti and Luchini (2007) in Table 1. An excellent agreement between them can be clearly seen from the table. The vorticity field of the unstable mode for the case of Re = 100 is shown in Fig. 4. The spatial distribution of vorticity in this figure is in consistency with that shown in Barkley (2006) (see figure 3 of Barkley, 2006).

4.2. Linear stability of the flow past an elastically mounted cylinder

Here we consider a canonical FIV system — flow past an isolated cylinder which is free to oscillate in the transverse direction. Three series of cases with different combinations of Reynolds number and density ratio, i.e., (Re = 40, $M^* = 10$), (Re = 60, $M^* = 20$) and (Re = 60, $M^* = 5$) are simulated here. In the first series, the reduced velocity varies in the range of 4.0–11.0, while in the other two series, the reduced velocity varies in the range of 3.0–11.0.

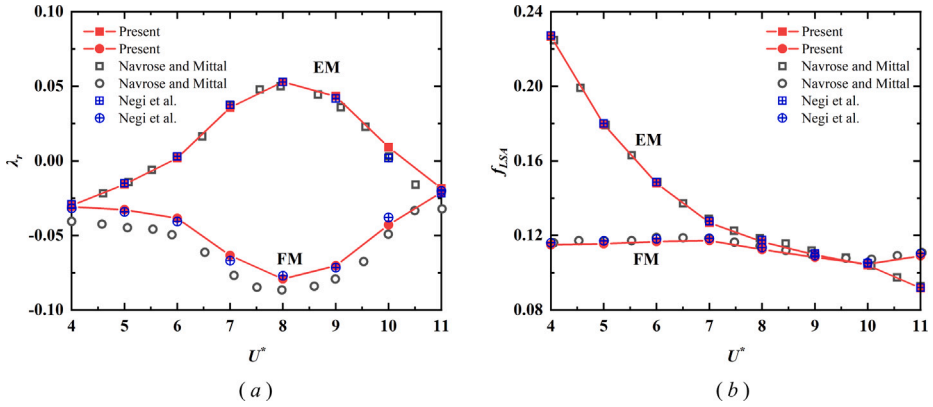

Fig. 5. Variations in (*a*) growth rate and (*b*) dimensionless frequency of the two least stable modes with reduced velocity for Re = 40 and $M^* = 10$.

The full linearized FSI equations (i.e., Eq. (6)) are solved in the linear stability analysis of the FIV system. The computational domain and mesh described in Section 4.1 are also used here. The boundary conditions at the four sides of the computational domain are the same as those described in Section 4.1. Please note that the base solution for this FIV system is the also same as that for the flow past a stationary cylinder.

In the first series (i.e., Re = 40, $M^* = 10$), the Reynolds number is below the critical value for the onset of vortex shedding in a stationary cylinder. The variations in growth rate and dimensionless frequency of the two least stable modes with reduced velocity are shown in Fig. 5(*a*) and Fig. 5(*b*), respectively. (The growth rate is the real part of the eigenvalue, while the dimensionless frequency is the imaginary part of the eigenvalue multiplied by a factor of $\frac{1}{2\pi}$.) The results indicate that only one mode of the FIV system becomes unstable within a certain range of reduced velocity. We refer to this mode as elastic mode (EM). The frequency of this mode scales as $1/U^*$ (the same way as the natural frequency of a spring–mass system does), hence its name. In the study by Navrose and Mittal (2016), it was found that the range of unstable EM mode coincided with the range of the lock-in regime. This is also confirmed by the result of the present study. The vorticity fields of the real and imaginary parts of EM mode at $U^* = 7$ (which lies in the unstable range) are shown in Fig. 6(*a*) and Fig. 6(*b*), respectively. We refer to the other mode (which is always stable in this series of cases), as the fluid mode (FM). The frequency of this mode only varies to a small extent around 0.12 with varying U^*. Such frequency value is close to that of the least stable mode in linear stability analysis of the flow past a stationary cylinder (see Giannetti and Luchini, 2007), hence its name.

In the second series (i.e., Re = 60, $M^* = 20$), the Reynolds number surpasses the critical value of vortex shedding in a stationary cylinder. The variations in growth rate and dimensionless frequency of the two least stable modes with reduced velocity are shown in Fig. 7(*a*) and Fig. 7(*b*), respectively. Similar to the previous series, one unstable EM mode can be identified in a certain range of U^*. However, unlike the previous series, an unstable FM mode can be identified in the entire range of U^*. The vorticity fields of the real part of EM and FM modes at $U^* = 7$ are shown in Fig. 8(*a*) and Fig. 8(*b*), respectively.

In the third series (i.e., Re = 60, $M^* = 5$), the Reynolds number also surpasses the critical value of vortex shedding in a stationary cylinder, while the density ratio is much lower than that of the second series. The variations in growth rate and dimensionless frequency of the two least stable modes with reduced velocity are shown in Fig. 7(*c*) and Fig. 7(*d*), respectively. Unlike the previous series, however, now it is not possible to classify the two leading modes as either EM mode or FM mode. We refer to these two modes as coupled modes, (i.e., FEM-I mode and FEM-II mode). Near the low-U^* end, FEM-I mode behaves like a fluid mode, while FEM-II mode acts as an elastic mode. Near the high-U^* end, the roles that the two modes play are reversed (FEM-I mode acts as an elastic mode, while FEM-II mode behaves like a fluid mode). From Fig. 7(*c*), it is also seen that there exists at least one unstable mode in the entire range of U^*. FEM-I mode exhibits instability near the low-U^* end and then transits into a stable mode as U^* increases. On the contrary, FEM-II mode is stable near the low-U^* end and transits into an unstable mode as U^* increases. The vorticity fields of the real part of FEM-I mode and FEM-II mode at $U^* = 6$ are shown in Fig. 8(*c*) and Fig. 8(*d*), respectively.

The growth rates and dimensionless frequency of the two least stable modes predicted in the present study are largely in consistency with those from the literature. For the series with a subcritical Re number, the growth rate matches very well with the result of Negi et al. (2020), and only deviates slightly from that of Navrose and Mittal (2016). For the two series with a supercritical Re number, the growth rate is in excellent agreement with the result of Sabino et al. (2020), and deviated slightly from that of Navrose and Mittal (2016). The flow fields of the two leading modes obtained here are also found to be in agreement with those from Navrose and Mittal (2016).

4.3. Linear stability of the flow past two tandem elastically mounted cylinders

The flow past two elastically mounted tandem cylinders is a more complex FIV system. Four series of cases are selected in the simulations of the present study. The values of parameters for these cases are listed in Table 2.

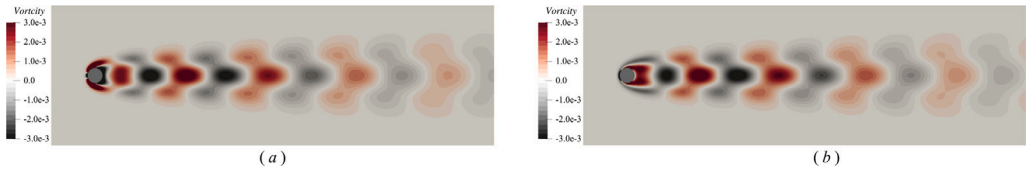

Fig. 6. Vorticity fields of the real (*a*) and imaginary (*b*) parts of the EM mode for (Re = 40, M^* = 10, U^* = 7).

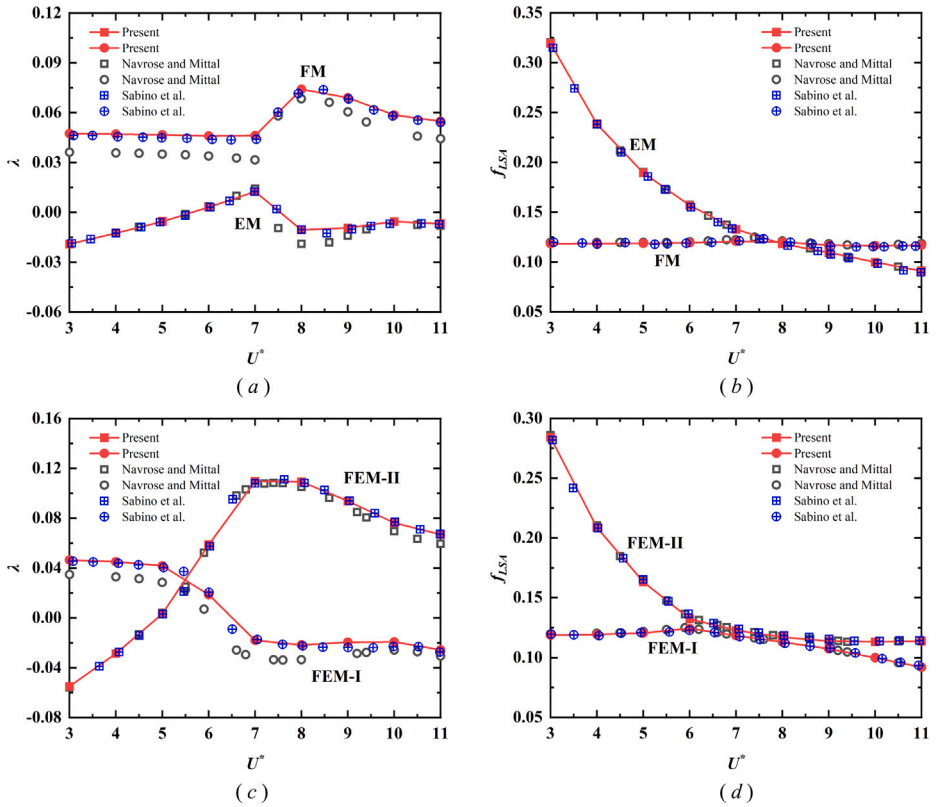

Fig. 7. Variations in (*a*)(*c*) growth rate and (*b*)(*d*) dimensionless frequency of the two least stable modes with reduced velocity at Re = 60 for (*a*)(*b*) M^* = 20 and (*c*)(*d*) M^* = 5.

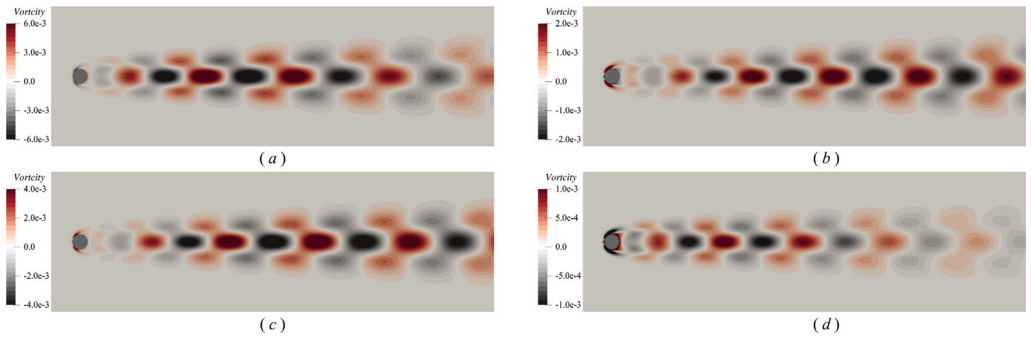

Fig. 8. Vorticity fields of the real part of (*a*) FM mode and (*b*) EM mode for (Re = 60, M^* = 20, U^* = 7), and (*c*) FEM-I mode and (*d*) FEM-II mode for (Re = 60, M^* = 5, U^* = 6).

Table 2
Values of control parameters for the flow past two tandem elastically mounted cylinders.

Series	Re	M^*	G	U^*
A	100	2.546	1.5	3.0–20.0
B	60	2.546	1.5	3.0–20.0
C	100	20.0	1.5	3.0–20.0
D	100	10.0	1.1	3.0–18.0

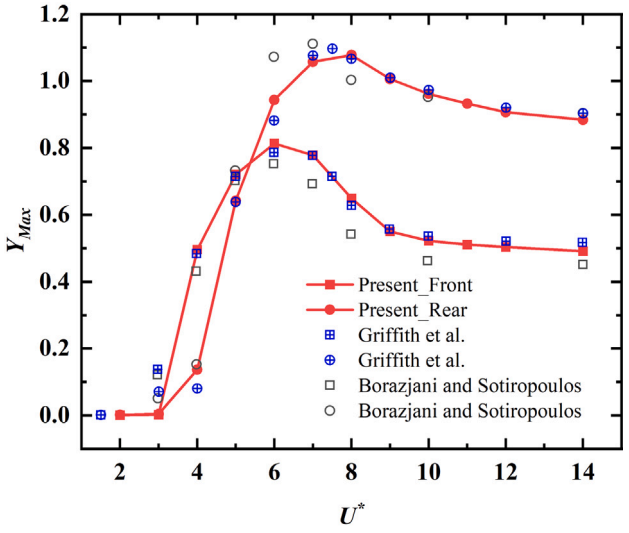

Fig. 9. Variations in maximum displacements of the front and rear cylinders with reduced velocity for Re=200, M^*=2.546, and G=1.5.

The reason for such selection is provided below. Series A has been investigated by Tirri et al. (2023), and the results were well documented. The inclusion of this series in the present study is mainly for the purpose of comparison. This series represents the situation with a supercritical Re number and a relatively low density ratio. The parameters in other three series lie in a range that has never been explored in the existing literature (in the sense of linear stability analysis). Series B represents the situation in which the Re number is reduced below the critical value and the density ratio is relatively low. (A discussion on the critical Re numbers in the flows past two tandem stationary cylinders will be presented in Section 4.3.2). Series C represents the situation with a supercritical Re number and a high density ratio. Series D represents the situation with a supercritical Re number, an intermediate density ratio, and a reduced gap ratio. Unlike the other three series, the galloping phenomenon was observed in this series of cases (see Sharma and Bhardwaj, 2023).

4.3.1. Code validation: nonlinear simulation

Prior to the linear stability analysis of the four series of cases listed in Table 2, nonlinear simulation is first conducted on another series of cases with Re = 200, $M^* = 2.546$, $G = 1.5$ and $2 \leq U^* \leq 14$. The results of the nonlinear simulation are compared with available data from the literature to further validate our code.

Fig. 9 shows the variations in maximum displacements of two cylinders with reduced velocity. The results from Griffith et al. (2017) and Borazjani and Sotiropoulos (2009) are also included for comparison. It is seen that the result of the present study is in excellent agreement with those from the literature. Fig. 10 shows the Lissajous curves of lift coefficient and dimensionless displacement at two reduced velocities ($U^* = 6,\ 8$). These curves bear a striking resemblance to those shown in figure 14 of Griffith et al. (2017).

4.3.2. Critical Reynolds numbers of the flows past two tandem stationary cylinders

Similar to that described in Section 4.1, linear stability analysis is performed on the flows past two tandem stationary cylinders to determine the critical Re numbers. Fig. 11 displays the variation in critical Reynolds number with the gap ratio. A good consistency between the result of this paper and the linear stability calculation from Carmo et al. (2008) is clearly seen. Additionally, at $G = 1.5$, the critical Reynolds number is found to be 74.1, which is very close to the result from Mizushima and Suehiro (2005) (i.e., $Re_c = 73.95$). The vorticity fields of the real parts of the leading modes for the flows past two tandem stationary cylinders at Re=100 with $G = 1.1$ and $G = 1.5$ are shown in Fig. 12.

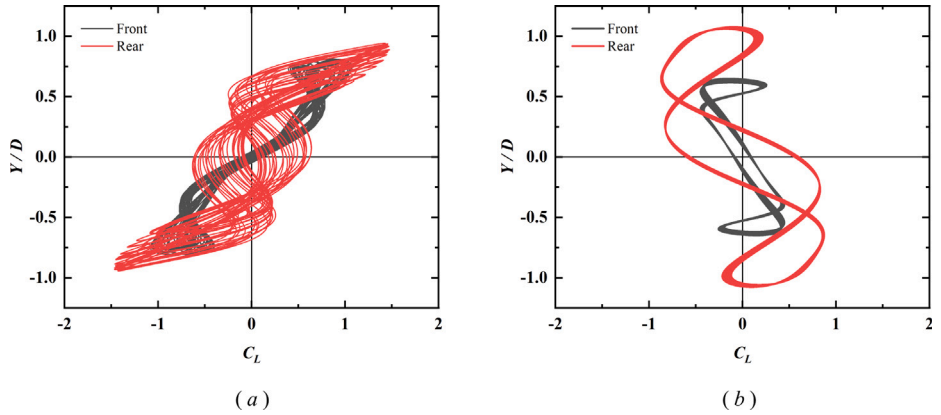

Fig. 10. Lissajous curves of lift coefficient and displacement for Re=200, M^*=2.546, G=1.5, and (a) U^* = 6, (b) U^* = 8.

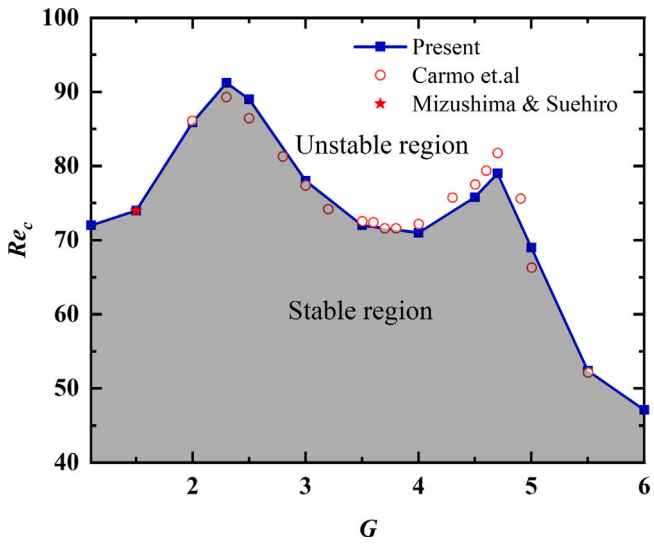

Fig. 11. Variation in critical Reynolds number with gap ratio for the flow past two tandem stationary cylinders.

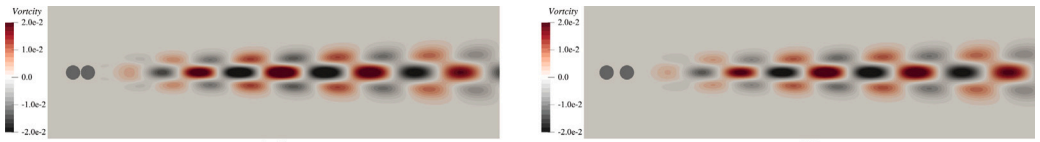

Fig. 12. Vorticity field of the real part of the leading mode for the flow past two tandem stationary cylinders at Re=100, with (a) G = 1.1 and (b) G = 1.5.

4.3.3. Linear stability analysis

The results of linear stability analysis of series A-D listed in Table 2 are presented in this subsection. To elucidate the connection between linear stability calculation and lock-in and galloping phenomena, nonlinear simulation is also conducted on the same cases. A mesh independent test and a domain independent test have been conducted to ensure that mesh resolution and domain size are sufficient for obtaining accurate results (see Appendix for the details).

For series A, the Reynolds number is 100, which lies in the supercritical range. The results of series A are shown in Fig. 13. Fig. 13(a) and Fig. 13(b) show the variations in growth rates and dimensionless frequencies of the two least stable modes with reduced velocity, respectively. Similar to Fig. 7(a) and Fig. 7(b), two leading modes can be identified as coupled modes (i.e., FEM-I mode and FEM-II mode). It is also evident that at least one unstable mode exists in the entire range of U^*. FEM-I mode behaves like a fluid mode and an elastic mode at the low-U^* and high-U^* ends, respectively. The behavior of FEM-II mode is just the other way around. At the high-U^* end, the growth rate of FEM-II mode approaches the value attained by FEM-I mode at the low-U^* end.

It is also found that near the position where two growth-rate curves intersect, the frequencies of two modes are also very close to each other. This is one typical characteristics which only shows up in cases with coupled modes.

At relatively low reduced velocities, the growth rates and dimensionless frequencies of the leading modes generally match well with those reported in Tirri et al. (2023). Some visible differences between the two results are found when the reduced velocity is increased. Such deviations are primarily attributed to different numerical strategies employed in the two studies. Unlike the present work, the leading eigenvalues of the linearized system were computed by a Jacobi-free approach in Tirri et al. (2023). The discrepancies in the leading eigenvalues were also reported in the investigation of the single-cylinder FIV system, when the result from Tirri et al. (2023) and those from Navrose and Mittal (2016) and Sabino et al. (2020)) were compared (see figure 4 of Tirri et al., 2023).

The variations in dimensionless maximum amplitude and frequency of the nonlinear responses with reduced velocity are shown in Fig. 13(*c*) and Fig. 13(*d*), respectively. It is seen that the lock-in regime in nonlinear responses does not correspond to the range of U^* over which either FEM-I mode or FEM-II mode becomes unstable. The low-U^* end of the lock-in regime coincides with the threshold U^* at which FEM-II mode becomes unstable. However, at the high-U^* end of the lock-in regime (near $U^* = 15.0$), the FEM-II mode remains unstable. Thus, we cannot affirm that it is the unstable FEM-II mode that leads to lock-in. The high-U^* end of the lock-in regime cannot be predicted by the stability property of FEM-I mode either, since FEM-I mode restores its stability at a much lower value of U^* (roughly 6.0). It is found that the high-U^* end of the lock-in regime is close to the position where FEM-I mode and FEM-II mode switch their roles (near $U^* = 14.0$). We tend to believe that the final desynchronization in nonlinear responses can be explained by the fact that the stable FEM-I mode takes over the role of an elastic mode from the unstable FEM-II mode. In Navrose and Mittal (2016), a similar finding was reported in the study of single-cylinder FIV system. They eventually confirmed that it was FEM-II mode that led to lock-in through a deep investigation on the distribution of energy between fluid and structure in the eigenmodes. Here we also stress that out of the lock-in regime, the amplitudes of cylinders are of order 10^{-3} (but no identically zero). This is in consistency with the finding that (at least) one unstable mode exists in the entire range of U^*. From Fig. 13(*b*) and Fig. 13(*d*), it is also observed that in most part of the lock-in regime, the frequencies in nonlinear responses and the two leading modes deviate noticeably from the natural frequency. This is because that the nominal natural frequency here refers to that of a spring–mass system placed in vacuum. At a low density ratio, due to the existence of strong added-mass effect, such frequency may deviate substantially from the true natural frequency of the FIV system (see Zhang et al., 2015).

The vorticity fields of the real parts of FEM-I mode and FEM-II mode at three different values of U^* are shown in Fig. 14. At a low reduced velocity, the vorticity filed of FEM-I mode closely resembles that of the stationary wake mode (see Fig. 12(*b*)), whereas the vorticity field of FEM-II mode bears similarities to EM mode of the single-cylinder FIV system (see Fig. 8(*b*)). Near the high-U^* end, the roles of FEM-I mode and FEM-II mode are exchanged. Specifically, FEM-I mode behaves like an elastic mode, while FEM-II mode behaves like a fluid mode. Such change in behaviors of the two modes is clearly displayed in this figure. For FEM-I mode, the region with large perturbation is shifted downstream. This is a typical feature of an elastic mode when U^* is increased (or when the frequency is reduced). For FEM-II mode, the vorticity field resembles that of the stationary wake mode. These findings in vorticity fields of the dual-cylinder FIV system are similar to those reported in the study of the single-cylinder FIV system (see Navrose and Mittal, 2016).

For series B, the Reynolds number is 60, which lies in the subcritical range. The results of series B are shown in Fig. 15. Fig. 15(*a*) and Fig. 15(*b*) show the variations in growth rates and dimensionless frequencies of the two least stable modes with reduced velocity, respectively. As can be seen here, the two leading modes are classified as FM mode and EM mode. FM mode remains stable in the entire range of U^*, while EM mode becomes unstable in a wide range of $5.2 \leq U^* \leq 17.0$. It is found that in the range of U^* where the frequencies of two modes are close to each other, the growth rates of them deviate significantly. This is the typical characteristics which is found in cases with uncoupled modes. The behaviors of FM mode and EM mode shown here are found to be similar to those of the single-cylinder FIV system at a subcritical Re (see Fig. 5). The only difference between them is that the range of U^* where the EM mode is unstable in this case is much wider than that in the case of single-cylinder system.

The variations in dimensionless maximum amplitude and frequency of the nonlinear response with reduced velocity are shown in Fig. 15(*c*) and Fig. 15(*d*), respectively. It is seen that the range of U^* over which EM mode becomes unstable coincides with that of the lock-in regime. Clearly, it can be concluded that it is the unstable EM mode that leads to lock-in. In contrast with series A, the amplitudes of cylinders are identically zero (to machine precision) out of the lock-in regime. This can be explained by the fact no unstable mode exists out of the lock-in regime. A similar finding was also reported in the study of single-cylinder FIV system at a subcritical Re (see Navrose and Mittal, 2016). Again, for the same reason aforementioned, in most part of the lock-in regime, the frequencies in the nonlinear response and two leading modes also deviate noticeably from the nominal natural frequency.

The vorticity fields of the real parts of EM mode at different U^* are shown in Fig. 16. As U^* increases, the frequency of EM mode decreases, which leads to an elongation of vortical structures.

For series C, the Re number is the same as that in series A (which lies in the supercritical range), but the density ratio is much higher. The results of series C are shown in Fig. 17. Fig. 17(*a*) and Fig. 17(*b*) show the variations in growth rates and dimensionless frequencies of the two least stable modes with reduced velocity, respectively. As can be seen, the two leading modes are also classified as EM mode and FM mode. The results of stability calculation of series A-C indicate that whether the leading modes are coupled or decoupled depends on both the Reynolds number and the density ratio. Unlike series B, the FM mode in series C is found to be unstable in the entire range of U^*. At the high-U^* end, the growth rate of FM mode approaches the value attained in itself at the low-U^* end. EM mode becomes unstable only in a narrow range of $5.7 \leqslant U^* \leqslant 7.5$. Similar to series B, in the range of U^* where the frequencies of two modes are close to each other, the growth rates of them deviate significantly.

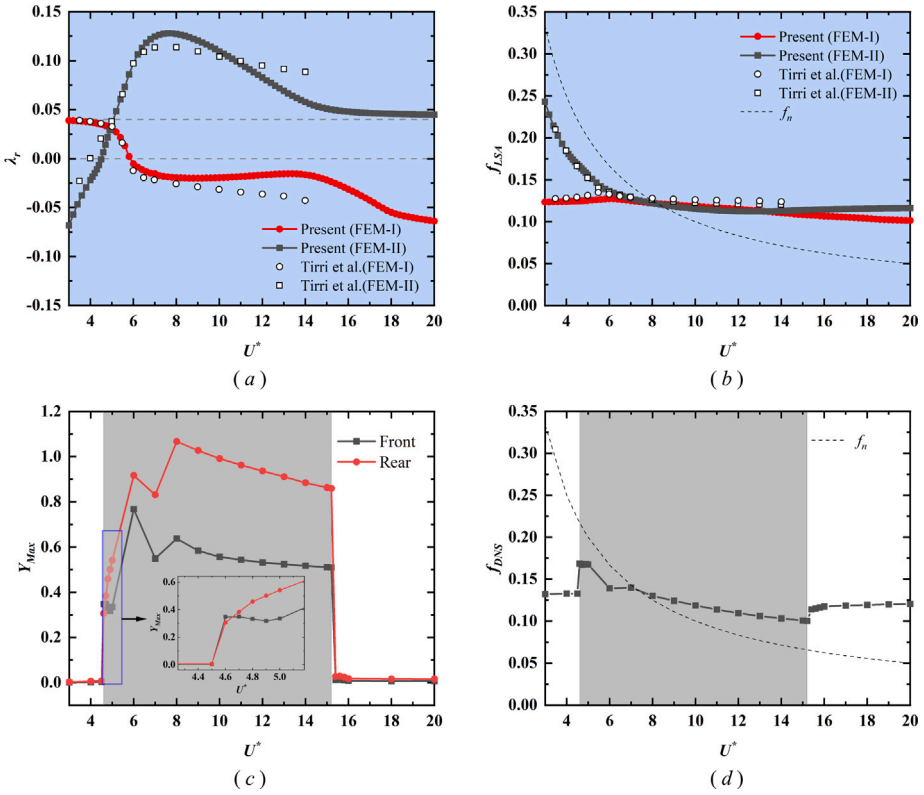

Fig. 13. Results of stability calculation and nonlinear simulation of series A (Re = 100, M^* = 2.546, G = 1.5): variations in (*a*) growth rate and (*b*) dimensionless frequency of the two least stable modes, variations in (*c*) dimensionless maximum amplitudes and (*d*) dimensionless frequencies of nonlinear responses with reduced velocity. The range of reduced velocity over which the system is linearly unstable in (*a*) and (*b*) is shaded in cyan. The range of reduced velocity for the lock-in regime in (*c*) and (*d*) is shaded in gray. (For interpretation of the references to color in this figure legend, the reader is referred to the web version of this article.)

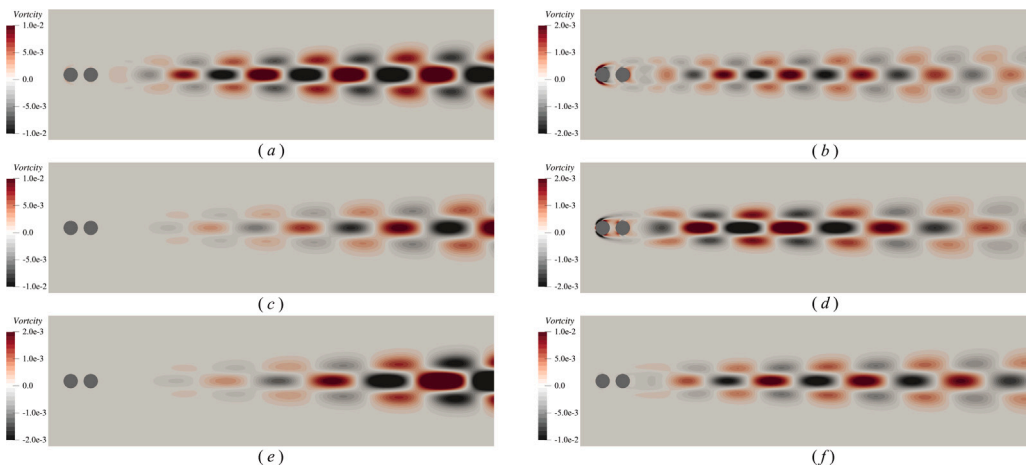

Fig. 14. Vorticity fields of the real part of (*a*, *c*, *e*) FEM-I mode and (*b*, *d*, *f*) FEM-II mode for series A (Re = 100, M^* = 2.546, G = 1.5) at (*a*, *b*) U^* = 5.4, (*c*, *d*) U^* = 12, and (*e*, *f*) U^* = 18.

The variations in dimensionless maximum amplitude and frequency of the nonlinear response with reduced velocity are shown in Fig. 17(*c*) and Fig. 17(*d*), respectively. It is seen that the low-U^* end of the lock-in regime coincides with the threshold U^* where EM mode becomes unstable. However, the high-U^* end of the lock-in regime (near U^* = 9.5) does not coincide with the value of U^* where stability of EM mode is restored (near U^* = 7.5). It is reasonable to believe that in the first part of the lock-in regime ($5.8 \le U^* \le 7.5$), lock-in is induced by the unstable EM mode, while in the second part ($7.5 \le U^* \le 9.5$), it is the unstable FM mode

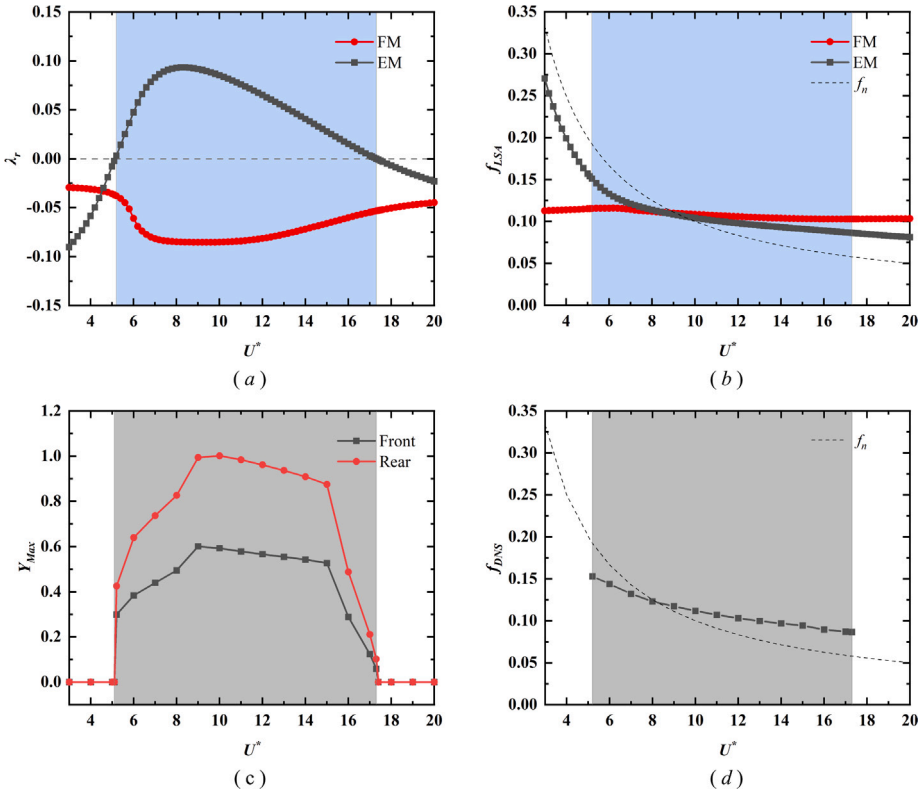

Fig. 15. Results of stability calculation and nonlinear simulation of series B (Re = 60, M^* = 2.546, G = 1.5): variations in (*a*) growth rate and (*b*) dimensionless frequency of the two least stable modes, variations in (*c*) dimensionless maximum amplitudes and (*d*) dimensionless frequencies of nonlinear responses with reduced velocity. The range of reduced velocity over which the system is linearly unstable in (*a*) and (*b*) is shaded in cyan. The range of reduced velocity of the lock-in regime in (*c*) and (*d*) is shaded in gray. (For interpretation of the references to color in this figure legend, the reader is referred to the web version of this article.)

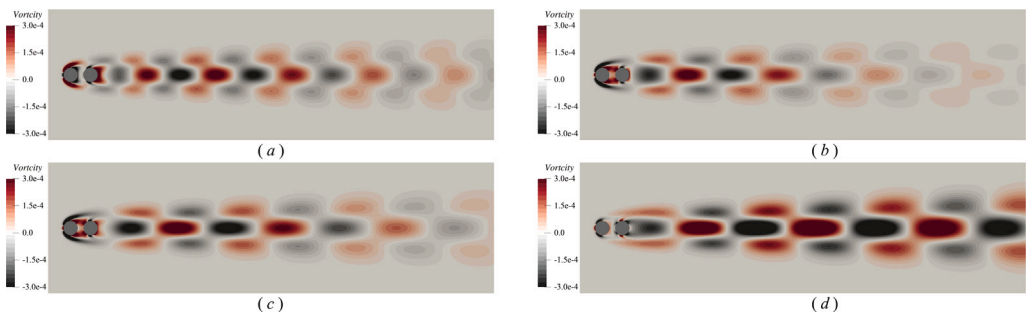

Fig. 16. Vorticity fields of the real part of EM mode for series B (Re = 60, M^* = 2.546, G = 1.5).

that leads to lock-in. The lock-in regime ends at a position where the frequency of FM mode and the natural frequency are sufficiently far apart from each other. In the study of single-cylinder FIV system by Zhang et al. (2015), these two distinct mechanisms which led to lock-in were termed as 'flutter-induced' and 'resonance-induced', respectively. Unlike series A and series B, in the lock-in regime of series C, the frequencies in both nonlinear responses and the two leading modes are very close to the natural frequency. This is because that the added-mass effect becomes insignificant when the density ratio is sufficiently high. Similar to series A, out of the lock-in regime, the amplitudes of cylinders are small but no identically zero. Again, this can be explained by the presence of an unstable mode in the entire range of U^*.

The vorticity fields of the real parts of FM mode and EM mode at different values of U^* are shown in Fig. 18. From this figure, it is evident that the change in the value of U^* has a negligible effect on the vorticity distribution of FM mode. The vorticity distribution of FM mode closely resembles that of the stationary wake mode (see Fig. 12(*b*)). Contrarily, when U^* increases, the regions with large perturbation in the EM mode are shifted downstream and with an elongation in the shape.

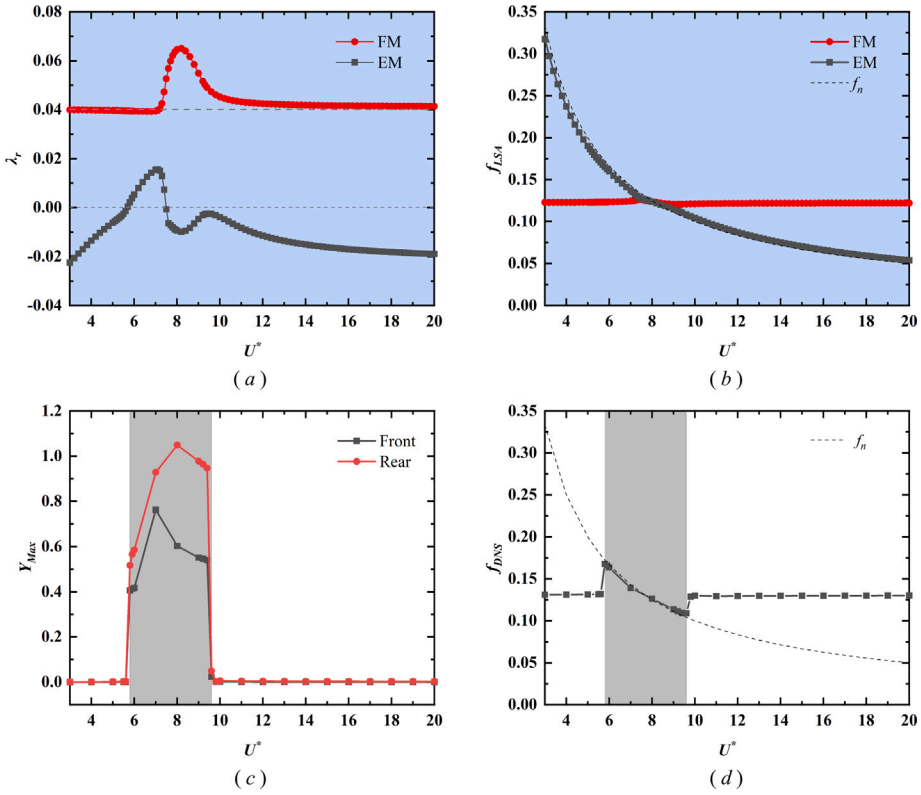

Fig. 17. Results of stability calculation and nonlinear simulation of series C (Re = 100, M^* = 20.0, G = 1.5): variations in (*a*) growth rate and (*b*) dimensionless frequency of the two least stable modes, variations in (*c*) dimensionless maximum amplitudes and (*d*) dimensionless frequencies of nonlinear responses with reduced velocity. The range of reduced velocity over which the system is linearly unstable in (*a*) and (*b*) is shaded in cyan. The range of reduced velocity for the lock-in regime in (*c*) and (*d*) is shaded in gray. (For interpretation of the references to color in this figure legend, the reader is referred to the web version of this article.)

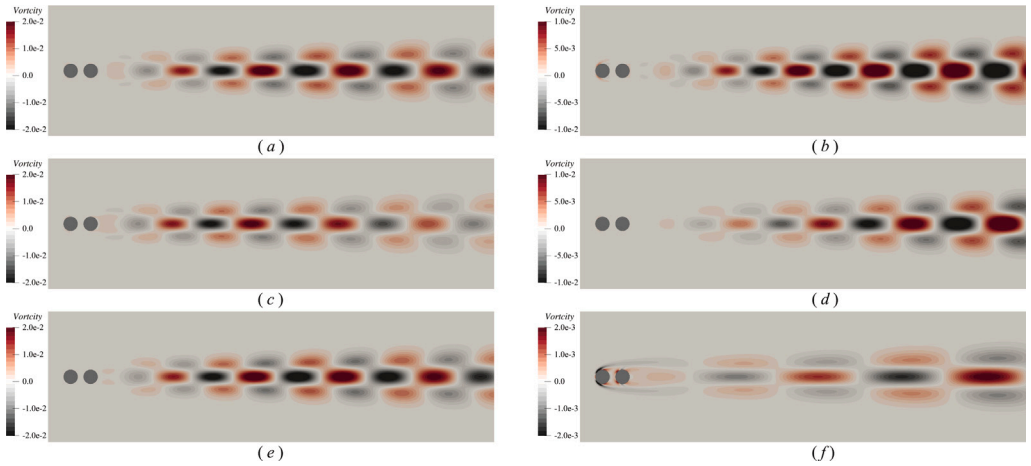

Fig. 18. Vorticity fields of the real part of (*a*, *c*, *e*) FM mode and (*b*, *d*, *f*) EM mode for series C (Re = 100, M^* = 20.0, G = 1.5).

For series D, the Re number is the same as that in series A (which also lies in the supercritical range), and the density ratio is moderate. Comparing with series A-C, the gap ratio is now reduced from 1.5 to 1.1. The results of series D are shown in Fig. 19. Fig. 19(*a*) and Fig. 19(*b*) show the variations in growth rates and dimensionless frequencies of the two least stable modes with reduced velocity, respectively. It is evident that two decoupled modes (EM mode and FM mode) can also be identified. FM mode remains unstable in the entire range of U^*. EM mode first becomes unstable at U^* = 5.2. In a narrow range near U^* = 8.2, the growth rate of EM mode attains a very small positive value close to zero. Unlike series C, however, with further increase in U^*,

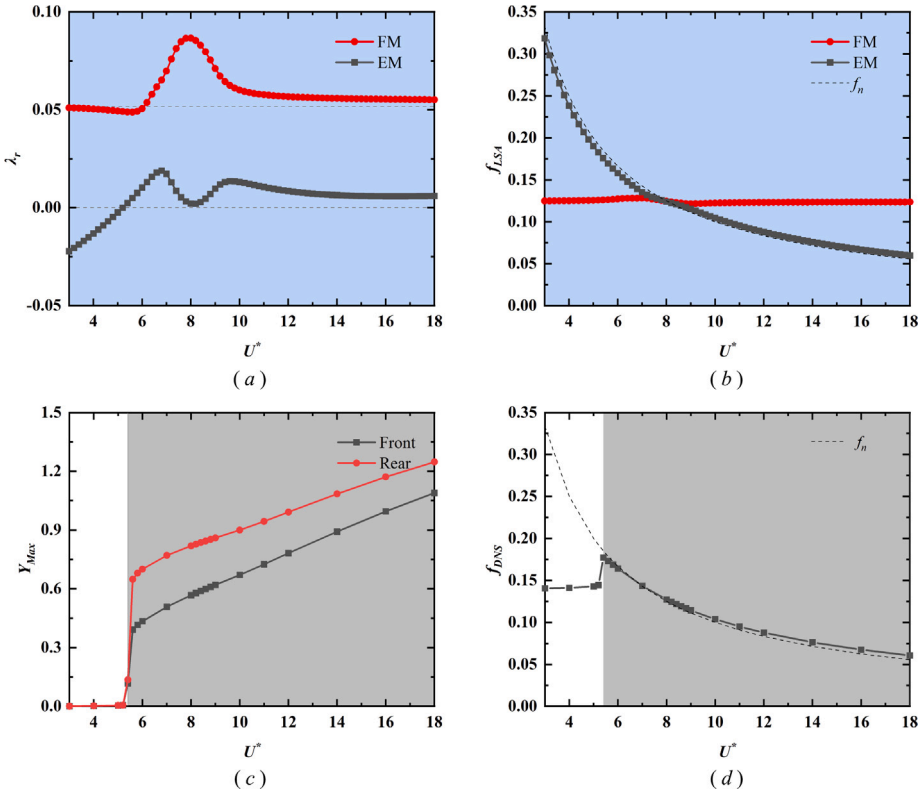

Fig. 19. Results of stability calculation and nonlinear simulation of series D (Re = 100, M^* = 10.0, G = 1.1): variations in (*a*) growth rate and (*b*) dimensionless frequency of the two least stable modes, variations in (*c*) dimensionless maximum amplitudes and (*d*) dimensionless frequencies of nonlinear responses with reduced velocity. The range of reduced velocity over which the system is linearly unstable in (*a*) and (*b*) is shaded in cyan. The range of reduced velocity for the galloping regime in (*c*) and (*d*) is shaded in gray. (For interpretation of the references to color in this figure legend, the reader is referred to the web version of this article.)

EM mode never becomes stable again. The growth rate of EM mode first increases and then slowly declines. It finally approaches a positive value at the high-U^* end.

The variations in dimensionless maximum amplitude and frequency of nonlinear response with reduced velocity are shown in Fig. 19(*c*) and Fig. 19(*d*), respectively. A galloping-like response of the cylinders is observed at high reduced velocities. More specifically, the amplitudes of both cylinders increase monotonically with reduced velocity after an initial jump. Such response is very similar to that observed in an elastically mounted D-section cylinder (see Zhao et al., 2018 and Sharma et al., 2022). The response of the cylinders predicted here is also in consistency with that obtained by the nonlinear simulation of Sharma and Bhardwaj (2023). From the stability calculation, it is seen that value of U^* for the initial jump in amplitude coincides with the threshold U^* where EM mode becomes unstable. Thus, the unstable EM mode is responsible for the initial jump in amplitude. In the range of U^* before the jump, the amplitudes are small but no identically zero. This can be explained by the presence of the unstable FM mode. Since the stability of EM mode is never restored for $U^* \geq 5.2$, it is reasonable to believe that the galloping-like behavior is also induced by the unstable EM mode. It is seen here that in the galloping regime the frequencies of nonlinear response and the EM mode are always locked onto the natural frequency. Similar to series C, this can be explained by insignificant added-mass effect at a relatively high density ratio.

Here we also stress that there exists a difference between the galloping phenomenon observed here and that observed in an isolated square cylinder where the galloping regime is clearly separated from the lock-in regime. The stability calculation of the square-cylinder case indicated that the galloping behavior near the high-U^* end can also be explained by the existence of unstable EM mode (see Li et al., 2019). However, in the square-cylinder case, the stability property of EM mode failed in predicting the onset point of either the lock-in regime or the galloping regime.

The vorticity fields of the real parts of FM mode and EM mode at different values of U^* are shown in Fig. 20. The vorticity fields of FM mode and EM mode closely resemble those obtained in series C (see Fig. 18). Please be noted that for series D, the elongated vortical structure of the unstable EM mode is responsible for the galloping-like response of the cylinders at high reduced velocities.

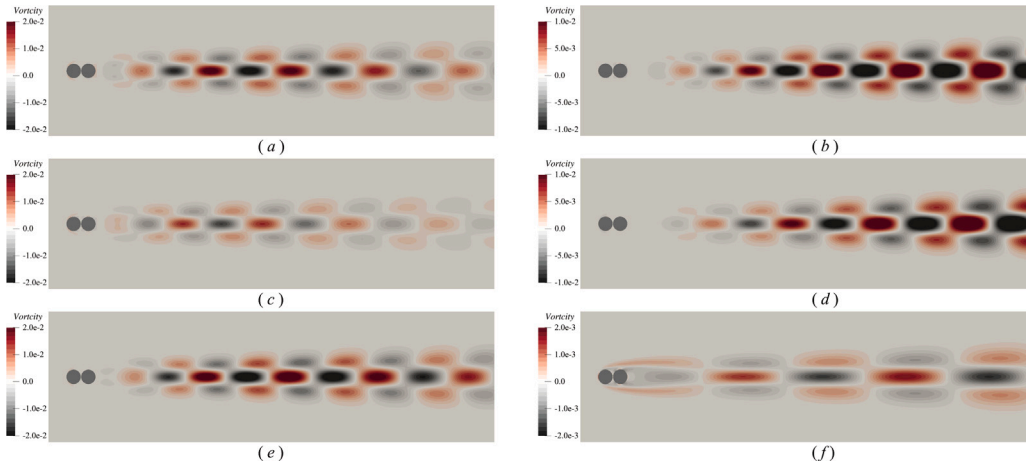

Fig. 20. Vorticity fields of the real part of (a, c, e) FM mode and (b, d, f) EM mode for series D (Re = 100, $M^* = 10.0$, $G = 1.1$).

5. Conclusions

A numerical technique in the framework of the immersed boundary method for performing global linear stability analysis of rigid-body-motion FSI problems is proposed. The Jacobian matrices associated with the perturbation of Lagrangian points in linearizing the coupled fluid–structure equations are derived numerically using a first-order finite difference scheme. The linear stability solver is first validated using two canonical cases, including the flow past a stationary cylinder and the flow past an isolated elastically mounted cylinder. The results obtained here are compared with the available data from the literature and an excellent agreement between them is achieved.

The solver is then applied to study the linear stability of the flow past two elastically mounted cylinders in tandem arrangement. Four series of cases with different combinations of Reynolds number, density ratio and gap ratio are investigated. Two leading modes are identified and the variations in growth rate and frequency of the leading modes with reduced velocity are examined.

The mechanisms of the lock-in and galloping phenomena observed in nonlinear simulation are also elucidated from the perspective of instabilities in the leading modes. In the first series, two coupled modes (FEM-I mode and FEM-II mode) are identified. The instability in FEM-II mode is responsible for the onset of lock-in, while the role switch between the two modes is responsible for the termination of lock-in. In the other three series, two uncoupled modes (EM mode and FM mode) are identified. In the second series, Re number lies in the subcritical range and it is the unstable EM mode that leads to lock-in. In the third series, Re number lies in the supercritical range and lock-in is related to two coexisting mechanisms, namely, 'flutter-induced' mechanism and 'resonance-induced' mechanism. The instabilities in EM mode and FM mode are linked with the former and the latter mechanisms, respectively. In the fourth series, Re number lies in the supercritical range and it is the unstable EM mode that leads to galloping.

CRediT authorship contribution statement

Zhiyu Zhang: Writing – review & editing, Writing – original draft, Visualization, Validation, Software, Methodology, Investigation, Formal analysis, Conceptualization. **Jianfeng Lu:** Writing – review & editing, Visualization, Validation, Software, Methodology, Investigation. **Xing Zhang:** Writing – review & editing, Writing – original draft, Supervision, Resources, Project administration, Investigation, Funding acquisition, Conceptualization.

Declaration of competing interest

The authors declare that they have no known competing financial interests or personal relationships that could have appeared to influence the work reported in this paper.

Data availability

Data will be made available on request.

Acknowledgments

This research was funded by the National Natural Science Foundation of China (NSFC) (under grant numbers 12172361 and 11988102) and the Chinese Academy of Sciences (under grant numbers XDA22040203 and XDB22040104). This research was also supported by the 'Open fund of State Key Laboratory of Hydraulic Engineering Intelligent Construction and Operation, Tianjin University'.

Table A.3
Effect of mesh resolution on maximum displacements of cylinders for (Re = 100, $M^* = 2.546$, $G = 1.5$, $U^* = 6.0$).

Mesh spacing	$\Delta h = D/25$	$\Delta h = D/50$	$\Delta h = D/100$
Y_{max}: front	0.7908	0.7677	0.7612
Y_{max}: rear	0.9808	0.9165	0.9011

Table A.4
Effect of mesh resolution on eigenvalues of two leading modes for (Re = 100, $M^* = 2.546$, $G = 1.5$, $U^* = 6.0$).

Mesh spacing	$\Delta h = D/25$	$\Delta h = D/50$	$\Delta h = D/100$
FEM-I mode	−0.0050+0.8049i	−0.0052+0.8004i	−0.0054+0.7985i
FEM-II mode	0.0926+0.8504i	0.0973+0.8571i	0.0987+0.8616i

Table A.5
Effect of domain size on maximum displacements of cylinders for (Re = 100, $M^* = 2.546$, $G = 1.5$, $U^* = 6.0$).

Domain size	$[56D \times 40D]$	$[80D \times 56D]$	$[104D \times 74D]$
Y_{max}: front	0.7683	0.7677	0.7670
Y_{max}: rear	0.9250	0.9165	0.9128

Table A.6
Effect of domain size on eigenvalues of two leading modes for (Re = 100, $M^* = 2.546$, $G = 1.5$, $U^* = 6.0$).

Domain size	$[56D \times 40D]$	$[80D \times 56D]$	$[104D \times 74D]$
FEM-I mode	−0.0082+0.8068i	−0.0052+0.8004i	−0.0045+0.7964i
FEM-II mode	0.0999+0.8595i	0.0973+0.8571i	0.0960+0.8560i

Appendix. Mesh and domain independence tests

To ensure that the mesh resolution and domain size are sufficient for obtaining accurate results in the simulations, two convergence tests are conducted.

A series of stretched Cartesian meshes are used in the mesh convergence tests (see Fig. 3). The parameter values used in the tests are: Re = 100, $M^* = 2.546$, $L = 1.5$, $U^* = 6.0$. Three different meshes resolutions are employed, with the finest grid spacing near the cylinders being $D/25$, $D/50$, and $D/100$, respectively. The impact of mesh resolution on the maximum displacements of the cylinders is presented in Table A.3. From this table, it is observed that the variations in maximum amplitudes of both cylinders are less than 2% as the grid spacing decreases from $D/50$ to $D/100$. Additionally, the effect of grid spacing on eigenvalues is shown in the Table A.4. The result indicates that the grid spacing of $D/50$ is sufficiently fine for obtaining accurate eigenvalues.

A domain size independence test is also conducted on the same case. From the Table A.5, it is observed that the domain size has very little effect on the maximum amplitudes of the cylinders. The stability calculations are found to be more sensitive to the domain size (as shown in Table A.6). Again, results from this table indicate that a domain size of $[80D \times 56D]$ is sufficiently large for obtaining accurate eigenvalues.

References

Assemat, P., Fabre, D., Magnaudet, J., 2012. The onset of unsteadiness of two-dimensional bodies falling or rising freely in a viscous fluid: a linear study. J. Fluid Mech. 690, 173–202.

Balay, S., Abhyankar, S., Adams, M.F., Benson, S., Brown, J., Brune, P., Buschelman, K., Constantinescu, E., Dalcin, L., Dener, A., Eijkhout, V., Faibussowitsch, J., Gropp, W.D., Hapla, V., Isaac, T., Jolivet, P., Karpeev, D., Kaushik, D., Knepley, M.G., Kong, K., Kruger, S., May, A., McInnes, L.C., Mills, R.T., Mitchell, L., Munson, T., Roman, J.E., Rupp, K., Sanan, P., Sarich, J., Smith, B.F., Zampini, S., Zhang, H., Zhang, H., Zhang, J., 2024. PETSc/TAO Users Manual. Tech. Rep. ANL-21/39 - Rev 3.20, Argonne National Laboratory.

Barkley, D., 2006. Linear analysis of the cylinder wake mean flow. Europhys. Lett. 75, 750–756.

Borazjani, I., Sotiropoulos, F., 2009. Vortex-induced vibrations of two cylinders in tandem arrangement in the proximity-wake interference region. J. Fluid Mech. 621, 321–364.

Cano-Lozano, J.C., Tchoufag, J., Magnaudet, J., Martínez-Bazán, C., 2016. A global stability approach to wake and path instabilities of nearly oblate spheroidal rising bubbles. Phys. Fluids 28, 014102.

Carmo, B.S., Meneghini, J.R., Sherwin, S.J., 2008. Possible states in the flow around two circular cylinders in tandem with separations in the vicinity of the drag inversion spacing. Phys. Fluids 22, 054101.

Colonius, T., Taira, K., 2008. A fast immersed boundary method using a nullspace approach and multi-domain far-field boundary conditions. Comput. Methods Appl. Mech. Eng. 197, 2131–2146.

Cossu, C., Morino, L., 2000. On the instability of a spring-mounted circular cylinder in a viscous flow at low Reynolds numbers. J. Fluids Struct. 14, 183–196.

Dolci, D.I., Carmo, B.S., 2019. Bifurcation analysis of the primary instability in the flow around a flexibly mounted circular cylinder. J. Fluid Mech. 880, R5.

Dolci, D.I., Carmo, B.S., 2022. Sensitivity of the least stable modes to passive control for a flow around an elastically mounted circular cylinder. Phys. Rev. Fluids 7, 083901.
Fernández, M.A., Tallec, P.L., 2003a. Linear stability analysis in fluid–structure interaction with transpiration. Part I: Formulation and mathematical analysis. Comput. Method. Appl. Mech. Eng. 192, 4805–4835.
Fernández, M.A., Tallec, P.L., 2003b. Linear stability analysis in fluid–structure interaction with transpiration. Part II: Numerical analysis and applications. Comput. Method. Appl. Mech. Eng. 192, 4837–4873.
Giannetti, F., Luchini, P., 2007. Structural sensitivity of the first instability of the cylinder wake. J. Fluid Mech. 581, 167–197.
Gómez, F., Clainche, S.L., Paredes, P., Hermanns, M., Theofilis, V., 2012. Four decades of studying global linear instability: progress and challenges. AIAA J. 50, 2731–2743.
Govardhan, R.N., Williamson, C.H.K., 2005. Vortex-induced vibrations of a sphere. J. Fluid Mech. 531, 11–47.
Goza, A., Colonius, T., Sader, J.E., 2018. Global modes and nonlinear analysis of inverted-flag flapping. J. Fluid Mech. 857, 312–344.
Griffith, M.D., David, D.L., Sheridan, J., Leontini, J.S., 2017. Flow-induced vibration of two cylinders in tandem and staggered arrangements. J. Fluid Mech. 833, 98–130.
Hayashida, H., Iwasa, Y., 1990. Aerodynamic shape effects of tall building for vortex induced vibration. J. Wind Eng. Ind. Aerodyn. 33, 237–242.
Hernandez, V., Roman, J.E., Vidal, V., 2005. SLEPc: A scalable and flexible toolkit for the solution of eigenvalue problems. ACM Trans. Math. Software 31, 351–362.
Hu, Z., Wang, J., Sun, Y., 2020. Cross-flow vibrations of two identical elastically mounted cylinders in tandem arrangement using wind tunnel experiment. Ocean Eng. 209, 107501.
Jauvtis, N., Govardhan, R.N., Williamson, C.H.K., 2001. Multiple modes of vortex-induced vibration of a sphere. J. Fluids Struct. 15, 555–563.
Kawai, H., 1992. Vortex induced vibration of tall buildings. J. Wind Eng. Ind. Aerodyn. 41, 117–128.
Kim, S., Alam, M.M., Sakamoto, H., Zhou, Y., 2009. Flow-induced vibrations of two circular cylinders in tandem arrangement. Part 1: Characteristics of vibration. J. Wind. Eng. Ind. Aerodyn. 97, 304–311.
Kim, D.K., Incecik, A., Choi, H.S., Wong, E.W.C., Yu, S.Y., Park, K.S., 2018. A simplified method to predict fatigue damage of offshore riser subjected to vortex-induced vibration by adopting current index concept. Ocean Eng. 157, 401–411.
Kou, J., Zhang, W., Liu, Y., Li, X., 2017. The lowest Reynolds number of vortex-induced vibrations. Phys. Fluids 29, 041701.
Li, X., Lyu, Z., Kou, J., Zhang, W., 2019. Mode competition in galloping of a square cylinder at low Reynolds number. J. Fluid Mech. 867, 516–555.
Lin, K., Wang, J., Zheng, H., Sun, Y., 2020. Numerical investigation of flow-induced vibrations of two cylinders in tandem arrangement with full wake interference. Phys. Fluids 32, 015112.
Meliga, P., Chomaz, J., 2011. An asymptotic expansion for the vortex-induced vibrations of a circular cylinder. J. Fluid Mech. 671, 137–167.
Mittal, S., Singh, S., 2005. Vortex-induced vibrations at subcritical Re. J. Fluid Mech. 534, 185–194.
Mizushima, J., Suehiro, N., 2005. Instability and transition of flow past two tandem circular cylinders. Phys. Fluids 17, 104107.
Moulin, J., Marquet, O., 2021. Flow-induced instabilities of springs-mounted plates in viscous flows: A global stability approach. Phys. Fluids 33, 034133.
Navrose, Mittal, S., 2016. Lock-in in vortex-induced vibration. J. Fluid Mech. 794, 565–594.
Negi, P.S., Hanifi, A., Henningson, D.S., 2020. On the linear global stability analysis of rigid-body motion fluid-structure-interaction problems. J. Fluid Mech. 903, A35.
Pfister, J.L., Marquet, O., 2020. Fluid-structure stability analyses and nonlinear dynamics of flexible splitter plates interacting with a circular cylinder flow. J. Fluid Mech. 896, A24.
Pfister, J.L., Marquet, O., Carini, M., 2019. Linear stability analysis of strongly coupled fluid-structure problems with the Arbitrary-Lagrangian-Eulerian method. Comput. Method. Appl. Mech. Eng. 355, 663–689.
Qin, B., Alam, M.M., Zhou, Y., 2019. Free vibrations of two tandem elastically mounted cylinders in crossflow. J. Fluid Mech. 861, 349–381.
Rajamuni, M.M., Thompson, M.C., Hourigan, K., 2020. Vortex dynamics and vibration modes of a tethered sphere. J. Fluid Mech. 885, A10.
Sabino, D., Fabre, D., Leontini, J.S., Jacono, D.L., 2020. Vortex-induced vibration prediction via an impedance criterion. J. Fluid Mech. 890, A4.
Sharma, G., Bhardwaj, R., 2023. Flow-induced vibrations of elastically coupled tandem cylinders. J. Fluid Mech. 976, A22.
Sharma, G., Garg, H., Bhardwaj, R., 2022. Flow-induced vibrations of elastically-mounted C- and D-section cylinders. J. Fluids Struct. 109, 103501.
Taira, K., Colonius, T., 2007. The immersed boundary method: a projection approach. J. Comput. Phys. 225, 2118–2137.
Tchoufag, J., Fabre, D., Magnaudet, J., 2014a. Global linear stability analysis of the wake and path of buoyancy-driven disks and thin cylinders. J. Fluid Mech. 740, 278–311.
Tchoufag, J., Magnaudet, J., Fabre, D., 2014b. Linear instability of the path of a freely rising spheroidal bubble. J. Fluid Mech. 751, R4.
Theofilis, V., 2017. Global linear instability. Ann. Rev. Fluid Mech. 43, 319–352.
Thorsen, M.J., Challabotla, N.R., Sævik, S., Nydal, O.J., 2019. A numerical study on vortex-induced vibrations and the effect of slurry density variations on fatigue of ocean mining risers. Ocean Eng. 174, 1–13.
Tirri, A., Nitti, A., Sierra-Ausin, J., Giannetti, F., de Tullio, M.D., 2023. Linear stability analysis of fluid-structure- interaction problems with an immersed boundary method. J. Fluids Struct. 117, 103830.
Uhlmann, M., 2005. An immersed boundary method with direct forcing for the simulation of particulate flows. J. Comput. Phys. 209, 448–476.
Vagnoli, G., Zampogna, G.A., Camarri, S., Gallaire, F., Ledda, P., 2023. Permeability sets the linear path instability of buoyancy-driven disks. J. Fluid Mech. 955, A29.
Wang, J., Geng, L., Ding, L., Zhu, H., Yurchenko, D., 2020. The state-of-the-art review on energy harvesting from flow-induced vibrations. Appl. Energy 267, 114902.
Wang, S.Z., Zhang, X., 2011. An immersed boundary method based on discrete stream function formulation for two- and three-dimensional incompressible flows. J. Comput. Phys. 230, 3479–3499.
Yang, X.L., Zhang, X., Li, Z.L., He, G.W., 2009. A smoothing technique for discrete delta functions with application to immersed boundary method in moving boundary simulations. J. Comput. Phys. 228 (20), 7821–7836.
Yao, W., Jaiman, R.K., 2017. Model reduction and mechanism for the vortex-induced vibrations of bluff bodies. J. Fluid Mech. 827, 357–393.
Zhang, W., Li, X., Ye, Z., Jiang, Y., 2015. Mechanism of frequency lock-in in vortex-induced vibrations at Low Reynolds Numbers. J. Fluid Mech. 783, 72–102.
Zhao, J., Hourigan, K., Thompson, M.C., 2018. Flow-induced vibration of D-section cylinders: an afterbody is not essential for vortex-induced vibration. J. Fluid Mech. 851, 317–343.
Zhu, X.J., He, G.W., Zhang, X., 2014. An improved direct-forcing immersed boundary method for fluid-structure interaction simulations. J. Fluids Eng. 136, 040903.
Zhu, H., Tang, T., Zhou, M., Cai, M., Gaidai, O., Wang, J., 2021. High performance energy harvesting from flow-induced vibrations in trapezoidal oscillators. Energy 236, 121484.